ARTICLE

Check for updates

Boride-derived oxygen-evolution catalysts

Ning Wang[1,2,10], Aoni Xu[2,10], Pengfei Ou [2,10], Sung-Fu Hung[3,10], Adnan Ozden[4], Ying-Rui Lu[5], Jehad Abed [2], Ziyun Wang [2], Yu Yan[2], Meng-Jia Sun[2], Yujian Xia[6], Mei Han[1], Jingrui Han[1], Kaili Yao[1], Feng-Yi Wu[3], Pei-Hsuan Chen[3], Alberto Vomiero [7,8], Ali Seifitokaldani[9], Xuhui Sun [6], David Sinton [3], Yongchang Liu [1✉], Edward H. Sargent [2✉] & Hongyan Liang[1✉]

Metal borides/borates have been considered promising as oxygen evolution reaction catalysts; however, to date, there is a dearth of evidence of long-term stability at practical current densities. Here we report a phase composition modulation approach to fabricate effective borides/borates-based catalysts. We find that metal borides in-situ formed metal borates are responsible for their high activity. This knowledge prompts us to synthesize NiFe-Boride, and to use it as a templating precursor to form an active NiFe-Borate catalyst. This boride-derived oxide catalyzes oxygen evolution with an overpotential of 167 mV at 10 mA/cm^2 in 1 M KOH electrolyte and requires a record-low overpotential of 460 mV to maintain water splitting performance for over 400 h at current density of 1 A/cm^2. We couple the catalyst with CO reduction in an alkaline membrane electrode assembly electrolyser, reporting stable C$_2$H$_4$ electrosynthesis at current density 200 mA/cm^2 for over 80 h.

[1] School of Materials Science and Engineering, Tianjin University, Tianjin 300350, China. [2] Department of Electrical and Computer Engineering, University of Toronto, 35 St George Street, Toronto, Ontario M5S 1A4, Canada. [3] Department of Applied Chemistry, National Chiao Tung University, Hsinchu 300 Taiwan, ROC. [4] Department of Mechanical and Industrial Engineering, University of Toronto, 5 King's College Road, Toronto, Ontario M5S 3G8, Canada. [5] National Synchrotron Radiation Research Center, Hsinchu 30076 Taiwan, ROC. [6] Institute of Functional Nano & Soft Materials (FUNSOM), Jiangsu Key Laboratory for Carbon-Based Materials and Devices, Soochow University, Suzhou, Jiangsu 215123, China. [7] Division of Materials Science, Department of Engineering Sciences and Mathematics, Luleå University of Technology, 97187 Luleå, Sweden. [8] Department of Molecular Sciences and Nanosystems, Ca' Foscari University of Venice, Via Torino 155, 30172 Venezia Mestre, Italy. [9] Department of Chemical Engineering, McGill University, Montreal, Quebec H3A 0C5, Canada. [10] These authors contributed equally: Ning Wang, Aoni Xu, Pengfei Ou, Sung-Fu Hung. ✉email: ycliu@tju.edu.cn; ted.sargent@utoronto.ca; hongyan.liang@tju.edu.cn

The design of active, stable, and cost-effective catalysts for the oxygen evolution reaction (OER) is critical to improving the full process efficiency in electrocatalytic systems, such as water splitting and CO_2/CO reduction reaction (CO_2/CORR) coupled with OER[1–4]. In these systems, approaches that use alkaline electrolytes have the benefit of increasing efficiency toward CO_2RR and CORR by suppressing the competing hydrogen evolution reaction (HER).

While there have been improvements in the activity of metal phosphides, sulfides, selenides, and borides/borates[5–8], achieving high electrocatalytic activity (>1 A/cm²) united with long-term stability (>100 h) remains an unmet need[9,10]. The lack of highly active and stable OER catalysts limits the performance and stability of electrosynthesis processes that rely on an OER anode (i.e., CO_2RR/CORR electrolysers) to production rates <100 mA/cm² and durations of <100 h. It remains an important task for the field to increase catalytic activity while achieving long-term durable and earth-abundant OER catalysts that operate at alkaline pH.

Metal borides/borates exhibit promising OER performance in high-pH regimes: incorporating highly electronegative boron diminishes the metal oxidation reaction energy barrier under a positive bias and assists with charge transfer[11,12]. To date, the durability of metal borides has been limited to <60 h at a modest current density of ~20 mA/cm²[2,13–15]. Thus far, to improve the activity and stability, significant efforts have been invested in charge-transfer enhancement and electronic structure optimization; however, we found herein that metal borides are prone to convert into metal borate under OER conditions, and thus to behave as the *operando* catalyst[16–18].

This knowledge prompted us to design metal borides as precursors to construct, in-situ, the metal borates that would endow the catalysts with activity and stability.
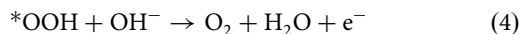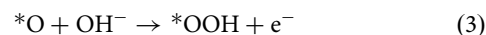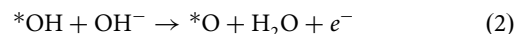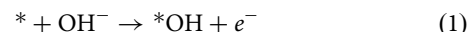
We focused on a NiFe-Boride compound and probed its phase transformation using *operando* X-ray spectroscopy during OER. We witnessed the in-situ transformation of NiFe-Boride to NiB_4O_7 and $FeBO_3$ phases on the catalyst surface during electrochemical activation. These results accord with DFT calculations which reveal that NiB_4O_7 species facilitate the step *O -> *OOH and enhance electrocatalytic activity toward OER.

Experimentally, we achieve an overpotential of 167 mV at 10 mA/cm² and stable water splitting performance of 400 h at 1 A/cm². Encouraged by its high activity and stability, we implement NiFe-Boride as the OER catalyst in a CORR membrane-electrode assembly (MEA) electrolyser that uses CO and H_2O to produce C_2H_4[19]. The CORR electrolyser based on the NiFe-Boride OER catalyst exhibited stable performance at 200 mA/cm² for over 80 h—maintaining a C_2H_4 energy efficiency of 19%—whereas this value is 17% for the CORR electrolyser that relies on a noble IrO_2 OER catalyst.

Results

Insight from computational studies into stable and active phases.
Noting that metal borides undergo phase transformation at highly oxidative potentials, we sought to calculate Pourbaix diagrams to evaluate the phase composition of NiFe-Boride ternary system at high potentials in alkaline electrolytes. Compared to the Pourbaix diagram of NiFe (Fig. 1a), we observe two new stable phases, $FeBO_3$ and NiB_4O_7, under a working potential ($U = 1.4—2$ V vs. RHE) at electrolyte pH (pH = 10—14) of alkaline OER in the Pourbaix diagram of NiFe-Boride (Fig. 1b), indicating that boron ions promote the new phases formation. The atomic configurations of these two new phases are shown in the Fig. 1c.

We carried out density functional theory (DFT) calculations to further explore the effects of these in-situ formed phases on the OER activity of NiFe catalyst. We first calculated the reaction energy of elementary steps and the overpotential for the OER based on the 4e-mechanism proposed by Nørskov et al. for water oxidation[20–22] with the reaction pathway:

$$* + OH^- \rightarrow *OH + e^- \qquad (1)$$

$$*OH + OH^- \rightarrow *O + H_2O + e^- \qquad (2)$$

$$*O + OH^- \rightarrow *OOH + e^- \qquad (3)$$

$$*OOH + OH^- \rightarrow O_2 + H_2O + e^- \qquad (4)$$

We cleaved the (100) facet of these two new phases to study the adsorption energy of various intermediates for OER, and thus to determine the theoretical overpotentials as an indicator for catalytic activity (Fig. 1d and Supplementary Fig. 1). The largest reaction energy (Step 2, deprotonation of *OH) was identified as the potential-determining step (PDS)[23], as shown in Fig. 1e, and the reaction energy was similar for both $FeBO_3$ (0.53 V) and NiOOH (0.56 V) at 1.23 V. In contrast, NiB_4O_7 shows a thermodynamic overpotential of 0.43 V, lowest among NiOOH, NiFeOOH and $FeBO_3$, which suggests that NiB_4O_7 phases are the active sites in NiFe-Boride that enable superior catalytic OER performance. We observed that the NiB_4O_7 shifts the PDS to the *OOH formation step at 1.23 V. We also obtained the similar calculation results at 1.40 V (Fig. 1e and Supplementary Fig. 2).

To account for other possible reaction mechanisms, we further studied the intramolecular oxygen coupling mechanism[24]: we found that Ni and Fe borate have increased activity compared to Ni and Fe (oxy)hydroxide (Supplementary Fig. 3). We also considered more sophisticated activity descriptors for multiple-electron processes, exploring the use of electrochemical-step symmetry index (ESSI) and the PDS at zero overpotential (G_{max})[25–27]: these results indicated higher OER activities of these NiFe-borate phases (Supplementary Table 1). Taken together, these results indicate that boron addition enables formation of new active phases, especially the Ni phase, in the pristine framework, thereby enhancing electrocatalytic activity toward OER.

Catalyst synthesis and characterization.
To test these hypotheses experimentally, we synthesized NiFe-Boride catalysts by a chemical reduction method (see Methods for details). Transmission electron microscopy (TEM), scanning electron microscopy (SEM), and X-ray diffraction (XRD) were conducted to investigate the structure, composition, and morphology of the NiFe-Boride catalyst. TEM and SEM images (Supplementary Figs. 4 and 5) revealed that catalysts the consisted of agglomerated nanoparticles. Elemental mapping analysis indicated that Ni, Fe, B, and O elements distribute homogeneously, without obvious separation or aggregation (Fig. 2a and Supplementary Fig. 6). A broad XRD diffraction peak between 40° and 50° indicates low crystallinity in the catalyst (Fig. 2b).

We further carried out X-ray photoelectron spectroscopy (XPS) to study the chemical state of the NiFe-Boride catalyst. XPS survey spectra show the presence of Ni, Fe, B, and O, which agrees well with the elemental mapping results (Supplementary Fig. 7). The B 1s spectrum obtained from the pristine sample was comprised of two peaks located at 192 eV and 187 eV, which are assigned to B-O and B^0/B-M species (Fig. 2c), respectively, indicating boride. The Ni and Fe K-edge X-ray absorption near-edge structure (XANES, Fig. 2d, e) revealed that NiFe-Boride possesses an electronic structure that differs from that of the control samples, indicating that the incorporation of boride leads
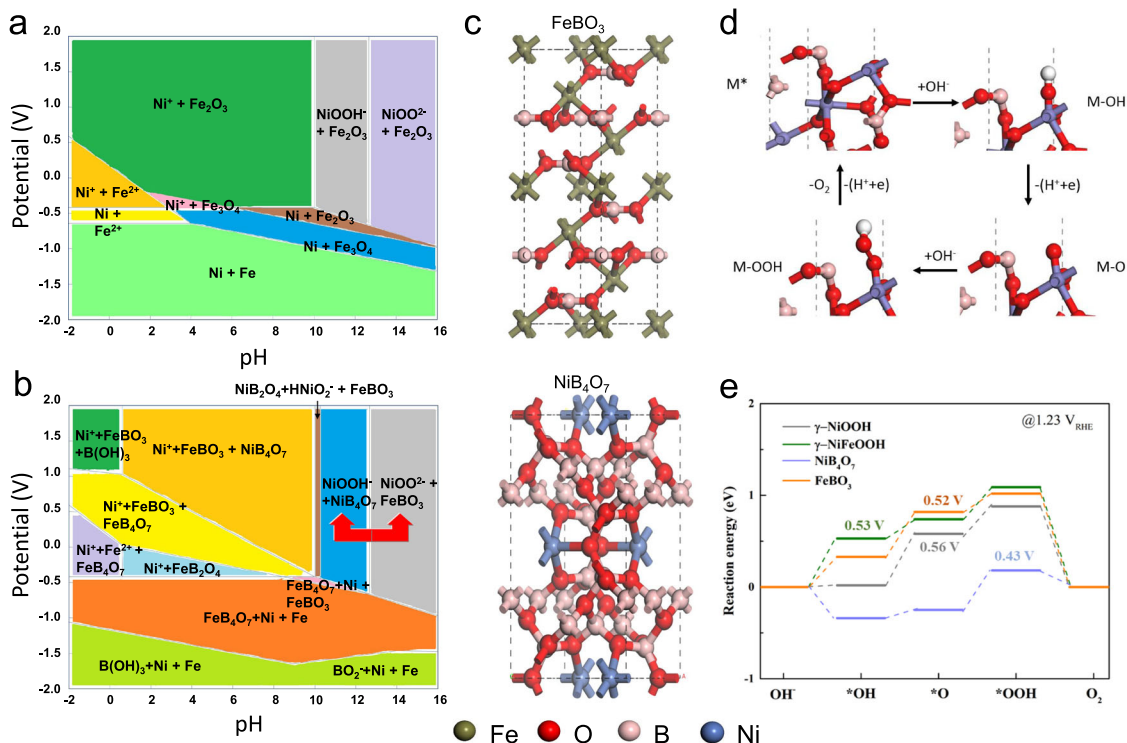
Fig. 1 Results of DFT calculations for NiFe-Boride catalysts. Pourbaix diagram of (**a**) NiFe and (**b**) NiFe-Boride; (**c**) The cell configurations of NiB_4O_7 and $FeBO_3$; (**d**) The schematic illustration of the 4-step OER pathway; (**e**) Predicted OER reaction energy diagram for NiB_4O_7, $FeBO_3$, γ-NiOOH, and γ-NiFeOOH in the alkaline electrolyte at 1.23 V vs. RHE.

to phase and structural changes. To probe the origins of these changes, we obtained a Fourier transform (FT) of the extended X-ray absorption fine structure (EXAFS, Fig. 2f, g) spectrum. NiFe-Boride showed two FT features: (1) the peak at ~1.5 Å represents the single-scattering path of M-O and (2) the peak at ~2.5 Å results from the single-scattering path of the closest neighboring transition metals around the metal cations (M-M) (the locations of the peaks match the locations of those in the NiFe control sample)[28]. The altered electronic structure suggests that the boride ions were incorporated into the NiFe framework via the formation of BO_x and $NiFeB_x$ species. Further investigations of the M-B peak remain a topic of interest.

Using inductively coupled plasma optical emission spectrometry (ICP-OES) analysis, we determined the molar ratio of Ni:Fe to be 1:1. Further analysis of the as-deposited system with the aid of energy-dispersive X-ray spectroscopy (EDS) indicated a 1:1 atomic ratio of Ni:Fe (Supplementary Fig. 8).

In-situ and ex-situ characterization. Using in-situ synchrotron radiation X-ray diffraction (SRXRD), we tracked changes in the crystal structure of catalysts during the OER process. We found that, prior to OER, the phase structure of the catalyst was $NiFeBO_4$ (see Supplementary Fig. 9 for the model structure). We found that $FeBO_3$ and NiB_4O_7 were formed under an applied potential (Fig. 3a, the standard patterns are provided in the Supplementary Fig. 10), consistent with in-situ formation of new phases in the NiFe-Boride catalyst during OER. We then carried out in-situ XAS to monitor the local electronic structure changes of the metal sites during the OER. The Ni and Fe K-edge XANES (Fig. 3b, c) spectra exhibited a positive energy shift, i.e., the valence states of Ni and Fe increased with the applied potential[29]. We analyzed the absorption edge energies in order to characterize the Ni/Fe valence states. Before OER, the valence states of Ni and Fe in NiFe-Boride were 1.91 and 2.73, respectively. During OER, the valence states of Ni and Fe increased to 1.98 and 2.95,

respectively (Supplementary Figs. 11–13). The ex-situ L-edge XAS results were in good agreement with this change: the reacted catalyst – compared to the pristine one – had a higher Ni^{3+} ratio and a similar $Fe^{2+/3+}$ ratio. The similarity in $Fe^{2+/3+}$ ratios indicates that Fe ions return to their initial states upon release of the applied potential. These results accord with the higher Ni^{3+} ratio in the reacted catalyst observed via O K-edge XAS (Supplementary Fig. 14).

We further analyzed the EXAFS spectra (Fig. 3d, e) to clarify the local structural variations associated with the Ni and Fe sites[30,31]. Under open circuit potential (OCP) in KOH electrolyte, the FT peaks demonstrated features similar to those obtained from the as-prepared catalysts. Once a positive bias was applied, the progressive FT peaks show that the original phase accomplishes some structural transformations. We conducted EXAFS fitting (Supplementary Tables 2–3 and Supplementary Figs. 15, 16) to determine the bond lengths of M-O and M-M (M is Ni or Fe). The interatomic distances of Ni-O and Ni-Ni(Fe) in as-prepared NiFe-Boride are 2.04 Å and 3.09 Å, respectively, while those measured during OER are 2.02 Å and 2.98 Å. The interatomic distances of Fe-O and Fe-Fe(Ni) in as-prepared NiFe-Boride are 2.23 Å and 3.22 Å, while those measured during OER are 1.92 and 3.05 Å. As oxidation and phase transformation progress, the M-O and M-M bonds become shorter than those at OCP. These results are in line with the generation of transition metal active sites with high valence[29]. The electronic structure of NiFe-Boride is different than that of Ni-Boride and Fe-Boride, indicating the presence of electronic communication between the Ni and Fe in M-M bonds (Supplementary Fig. 17).

We carried out XPS to study the local evolution of chemical state and electronic structure before vs. after OER, with all peaks calibrated using C 1s (Supplementary Fig. 18). High-resolution XPS in Ni 2p region showed two main peaks of Ni^{2+} $2p_{3/2}$ and Ni^{2+} $2p_{1/2}$ located at 855.4 and 873.3 eV (Fig. 3f), accompanied by satellite peaks centered at 861.2 and 879.4 eV[32]. In the Fe 2p
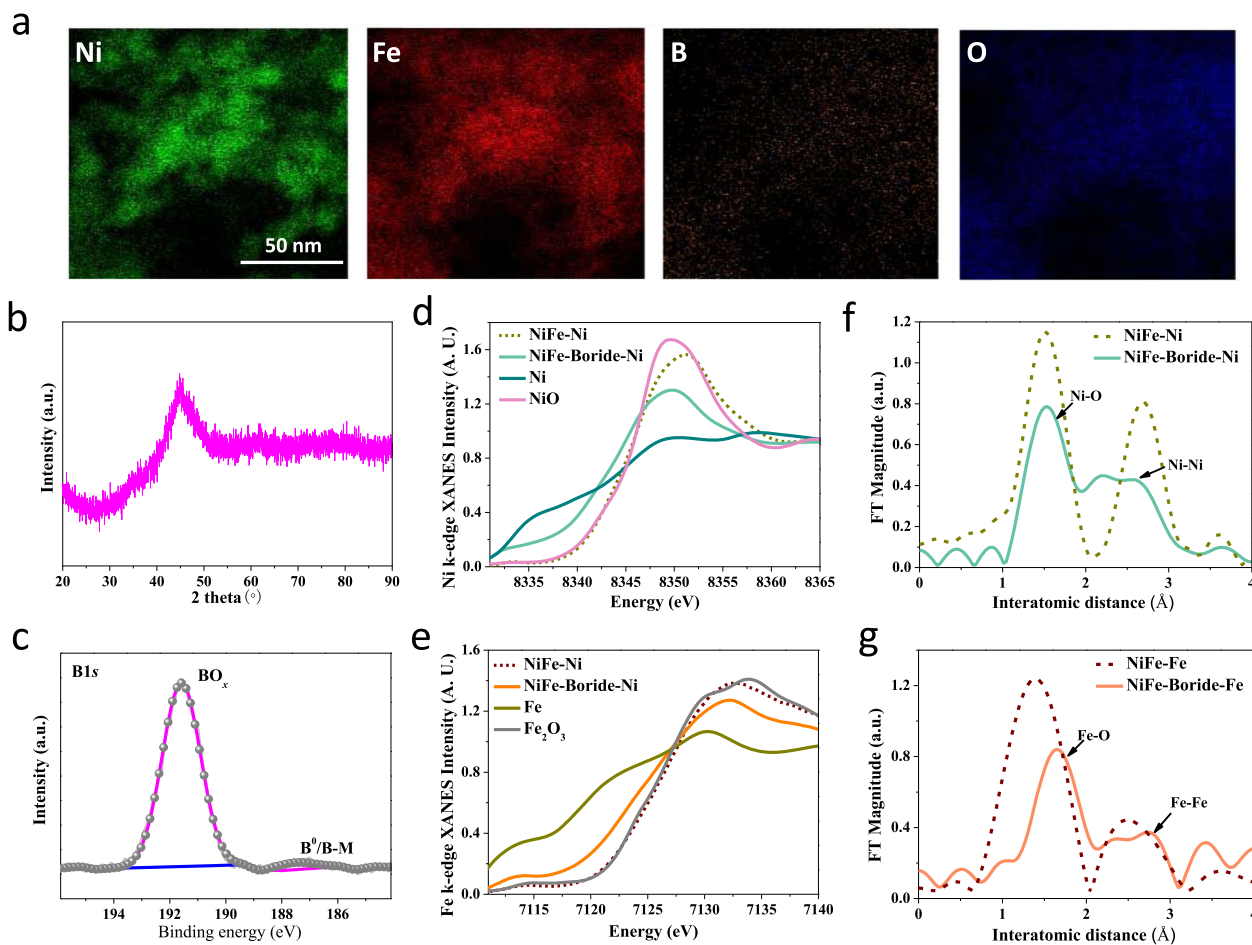
Fig. 2 Characterization of the morphology and composition of NiFe-Boride catalyst. (a) Elemental mapping analysis, showing the uniform, uncorrelated spatial distribution of Ni, Fe, B and O. (**b**) XRD patterns. (**c**) B 1s XPS spectrum of fresh NiFe-Boride sample. The Ni and Fe K-edge XANES (**d**) and (**e**) and EXAFS (**f**) and (**g**) data for fresh NiFe-Boride and control samples.

region, two main peaks located at 710.7 and 724.6 eV were assigned to Fe $2p_{3/2}$ and Fe $2p_{1/2}$ (Fig. 3g). We noted minor peaks centered at ~851.9 and 706.1 eV in the Ni 2p and Fe 2p spectra of fresh catalyst, suggesting the existence of Ni-B and Fe-B bonds in NiFe-Boride (Fig. 3f, g)[33], consistent with EXAFS. The B 1s spectrum consists of two peaks corresponding to B-O and B^0/B-M species. Upon completion of electrochemical activation during OER, negative chemical shifts in the binding energy of Ni 2p and Fe 2p peaks were observed compared to pristine NiFe-Boride. These negative shifts indicated the modulation of the surface electronic structure through the oxidation process, in accordance with the positive shift in the peak position of B-O bonds (Supplementary Fig. 19). Harsh oxidative conditions during OER converted the M-B species into oxides and hydroxides, evidenced by the disappearance of Ni-B, Fe-B, and B^0/B-M signals.

In sum, NiFe-Boride acts as a precursor that phase transforms at highly oxidative potentials, leading to the formation of stable $FeBO_3$ and NiB_4O_7 phases during the OER process.

Electrocatalytic performance. The OER performance of NiFe-Boride and controls on Ni foam was examined in 1 M KOH electrolyte using a three-electrode cell at room temperature (see Methods). As shown in linear sweep voltammetry (LSV, Fig. 4a) curves, the overpotential of NiFe-Boride catalyst at 10 mA/cm²[2,34] and without iR compensation is 167 mV. This is lower than the 200 mV and 189 mV obtained for sol-gel NiFe and IrO_2, respectively (Supplementary Table 4). Rotating ring disk measurements

show a similar trend: NiFe-Boride enables higher-rate water oxidation performance than in control catalysts (Supplementary Fig. 20). To seek insight into the effect of in-situ active sites on performance, we compared the catalytic activity between annealed and pristine catalysts. The annealed catalysts have lower performance, consistent with an activity-promoter role for the in-situ formed active sites (Supplementary Figs. 21-22). A Ni:Fe ratio of 1:1 (Supplementary Fig. 23 and Table 5) leads to the lowest overpotential. We determined the Tafel slope (Fig. 4b), finding 25 mV/dec for the NiFe-Boride catalyst, lower than for IrO_2 (41 mV/dec) and NiFe (66 mV/dec). The lower Tafel slope value indicating rate-determining step is shifted from the *O step to the *OOH formation step[35,36]. Compared to benchmark OER catalysts from literature, NiFe-Boride shows higher catalytic performance in terms of overpotential at 10 mA/cm² and Tafel slope in the alkaline solution (Fig. 4c). From Nyquist plots based on electrochemical impedance spectroscopy (EIS, Fig. 4d) at applied potential 1.45 V vs. RHE reveal that NiFe-Boride exhibits a lower charge-transfer resistance (R_{ct}) than does either NiFe or IrO_2.

We then used electrochemically active surface area (ECSA) obtained via the double-layer capacitance (C_{dl}, Supplementary Fig. 24) technique to estimate a normalized current density[37]. This for NiFe-Boride is 7.5 mA/cm², >2x greater than that in IrO_2, and 4x greater than in NiFe catalysts, at 1.45 V vs. RHE (Supplementary Fig. 25). *IR*-corrected LSV excludes the effect of ionic conductivity on performance: the NiFe-Boride catalyst showed an iR-corrected overpotential of 160 mV at 10 mA/cm²
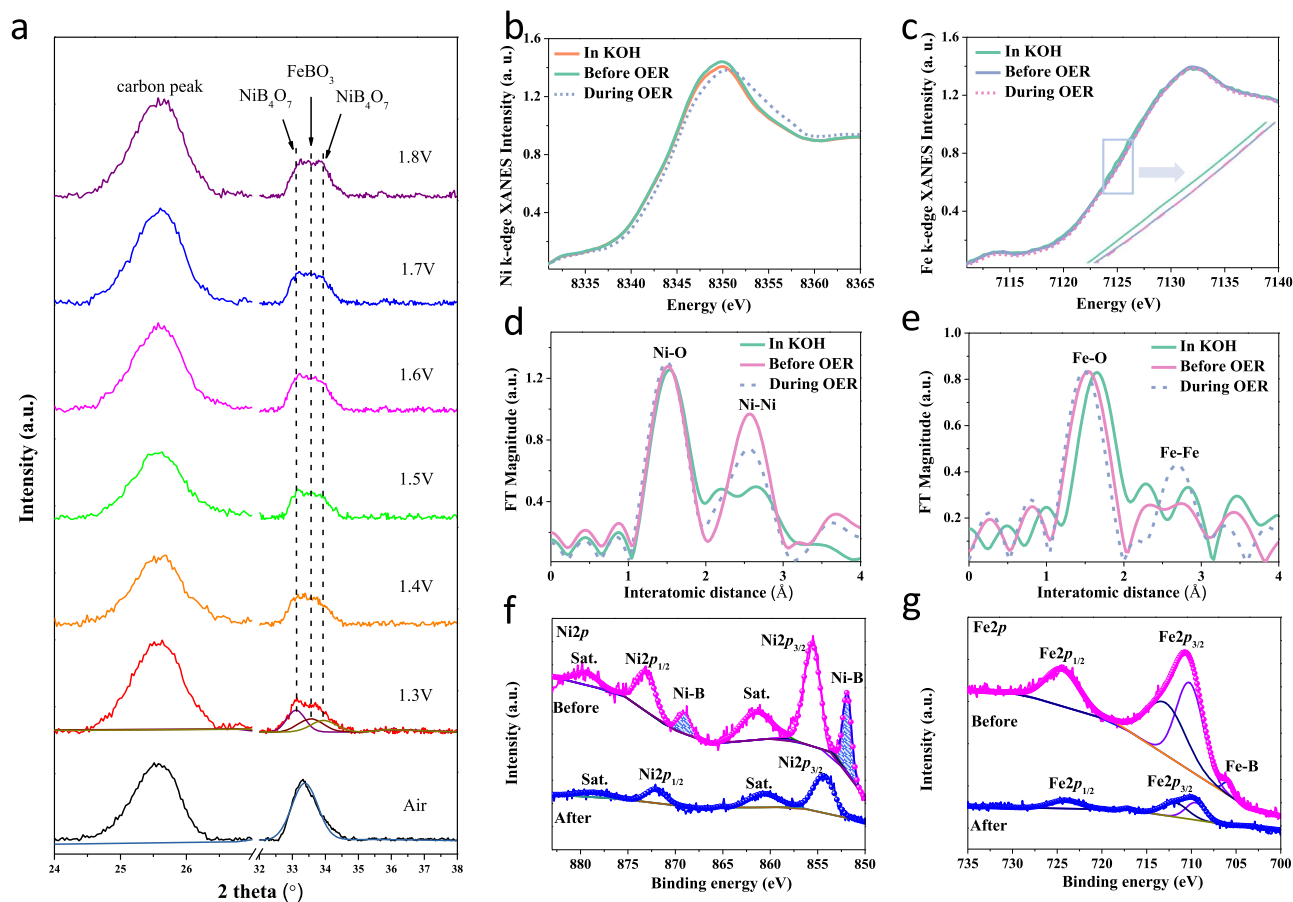
Fig. 3 Ex/in-situ characterization of as-prepared NiFe-Boride catalyst. a In-situ SRXRD patterns of the catalyst during the OER test in 1 M KOH electrolyte; The in-situ Ni and Fe *K*-edge XANES (**b**) and (**c**) and EXAFS (**d**) and (**e**) data of NiFe-Boride during the LSV process in 1 M KOH aqueous electrolyte. The in-situ applied voltages before and during the OER are 1.2 and 1.4 V vs. RHE, respectively. **f** Ni 2*p* and (**g**) Fe 2*p* XPS spectra for fresh and post-OER samples.

on Ni foam (Supplementary Fig. 26), which is 35 and 23 mV lower than for NiFe and IrO$_2$.

We measured the stability of the best-performing NiFe-Boride catalyst at 20 mA/cm^2 and found that the increase in potential was less than 10 mV after 100 h of continuous water splitting (Fig. 4e), more stable than the control and reference samples (Fig. 4f). We obtained stability at 1 A/cm^2, finding that catalysts enable stable operation of 400 h with an overpotential of 460 mV without degradation (Fig. 4g). B 1 s XPS results indicate that the B concentration gradually decreases over the first 100 h but then remains constant over the ensuing 300 h (Supplementary Fig. 27). The Faradaic efficiency (FE) toward O$_2$ remains 98 ± 2% over the first 400 h, excluding a major current contribution associated with materials corrosion.

To investigate further the potential relevance of these catalysts to future systems, we implemented NiFe-Boride as the OER catalyst in a CORR MEA electrolyser that produces C$_2$H$_4$ from CO and H$_2$O (Supplementary Fig. 28). The CORR electrolyser exhibited stable performance at 200 mA/cm^2 for over 80 h, maintaining a cell potential of −2.85 V, a C$_2$H$_4$ FE of 45%, and a C$_2$H$_4$ energy efficiency of 19%. Under similar operating conditions, the cell potential for the IrO$_2$ OER catalyst-based electrolyser was −3.06 V, which is ~200 mV higher than in the NiFe-Boride OER catalyst-based system (Fig. 4h and Supplementary Fig. 29), corresponding to a C$_2$H$_4$ energy efficiency of 17%. Using XPS and EDS line scanning, we found that Ni, Fe, and B elemental signals remained following the stability study (Supplementary Figs. 30 and 31)., i.e., the borate remained in the NiFe.

Discussion

Starting from DFT calculations, we saw that the phase transformation of NiFe-Boride to NiFe-Borate can be activated under OER potentials in OER. The in-situ formed new phase (NiB$_4$O$_7$) can function as active site to facilitate *O -> *OOH, enhancing the electrocatalytic activity of NiFe-Boride in OER. We evaluated the electrochemical performance of the catalyst and found that NiFe-Boride possesses a Tafel slope of 25 mV/dec and an overpotential of 167 mV at current density 10 mA/cm^2 in 1 M KOH solution, outperforming benchmark NiFe oxide. The in-situ formed NiFe-Borate phases are confirmed via *operando* spectroscopies. The catalyst demonstrates stable performance over 400 h at 1 A/cm^2 in water splitting. We further showcased 80 h of stable C$_2$H$_4$ electrosynthesis using a NiFe-Boride OER catalyst in a CORR MEA electrolyser, with a ~200 mV lower cell potential compared to MEA electrolysers based IrO$_2$ OER catalysts.

Methods

I.1. Chemicals. Iron (III) chloride (FeCl$_3$), nickel (II) chloride hexahygrate (NiCl$_2$·6H$_2$O), Sodium borohydride (NaBH$_4$), ethanol (≥99.5%) and acetone (≥99 %) were purchased from Sigma-Aldrich. Iridium (IV) oxide dehydrate (99.99%) was purchased from Alfa Aesar®. All chemicals were used without further purification.

I.2. Synthesis of NiFe-Boride and control catalysts. Th NiFe-Boride catalysts were synthesized using a modified chemical reduction method. NiCl$_2$·6H$_2$O (332.8 mg) and anhydrous FeCl$_3$ (227.1 mg) were first dissolved in deionized water (DI, 2 mL) in a vial. A solution of NaBH$_4$ (2 mL, 5 M) in water was prepared in a separate vial. All solutions mentioned above were cooled in an ice bath for 10 min
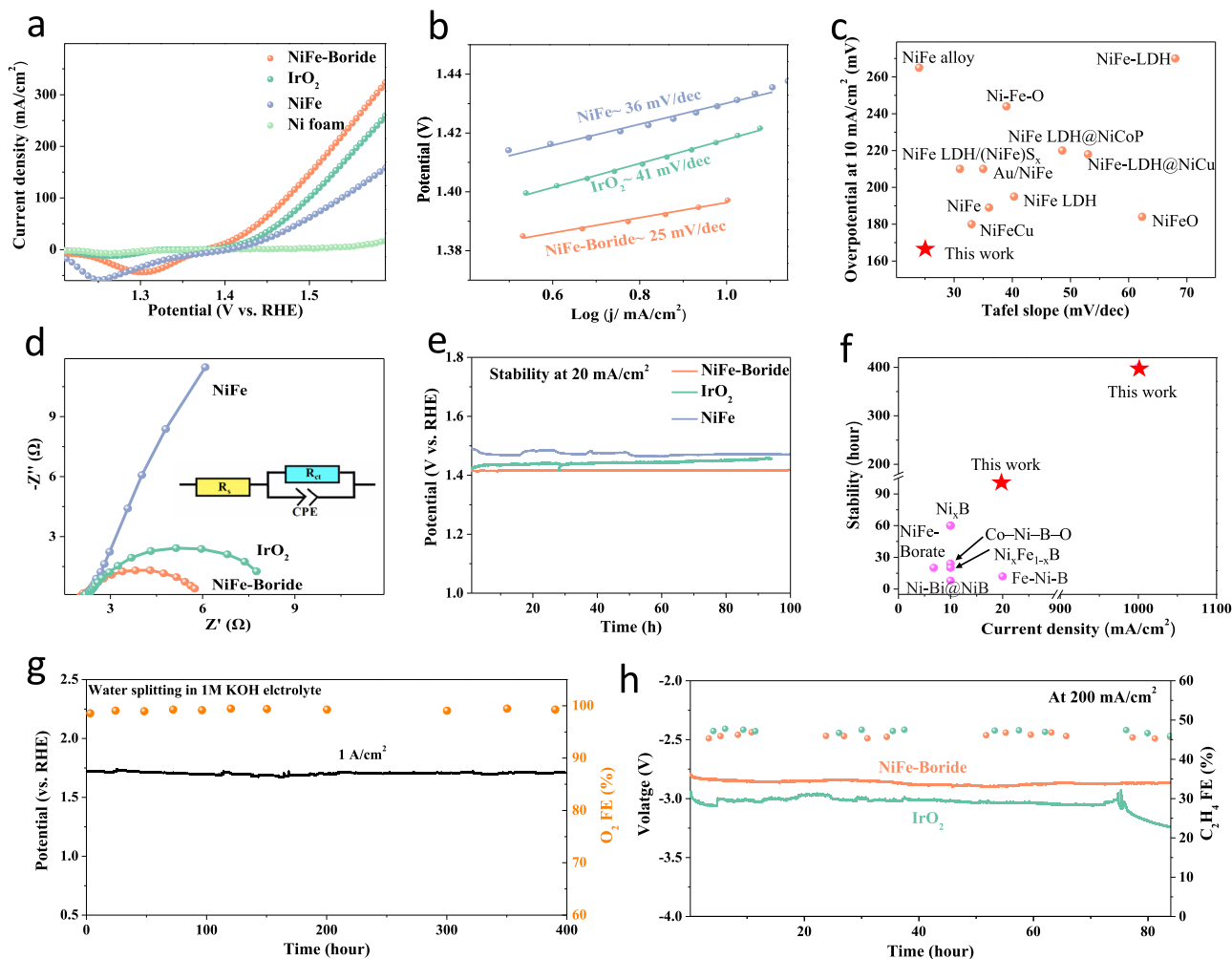
Fig. 4 Performance of NiFe-Boride catalyst and controls in a three-electrode configuration in 1M KOH aqueous electrolyte. a OER LSV polarization curves for catalysts loaded on Ni foam without *iR* correction. **b** The corresponding Tafel plot of catalysts. **c** Comparison of Tafel slope and overpotential required to achieve 10 mA/cm^2, with references all measured in alkaline medium[47-57]. **d** EIS data for NiFe-Boride and controls in three-electrode configuration. The data were collected at 1.45 V vs. RHE. The inset provides the equivalent circuit: R_s series resistance, R_{ct} charge-transfer resistance, and CPE constant-phase element related to the double-layer capacitance. **e** Chronopotentiometric curves obtained from the NiFe-Boride catalyst on Ni foam electrode at a constant current density of 20 mA/cm^2. **f** Comparison of stability at different current density, with references all measured in alkaline medium[13-15,33,58]. **g** Operating voltage and O$_2$ FE at constant 1 A/cm^2 current density in a three-electrode configuration in 1 M KOH aqueous electrolyte. **h** The operating voltage and ethylene FE were monitored at constant 200 mA/cm^2 in a membrane-electrode assembly device. NiFe-Boride and IrO$_2$ supported on titanium felt were used as the anodes. The high surface area Cu catalyst on hydrophobic carbon paper acted as cathode. Humidified CO was flowed through the gas channels in the cathode, and 2 M aqueous KOH solution was flowed through channels in the anode.

to prevent uncontrolled hydrolysis and consideration which may lead to the formation of the precipitate. The Ni and Fe precursors were then added dropwise to NaBH$_4$ to form a black solution. Finally, the prepared solution was further washed and centrifuged with water and ethanol three times before vacuum drying. The samples of different Ni:Fe ratios were synthesized by changing the Ni and Fe precursors concentration.

NiFe catalysts were synthesized using a modified aqueous sol-gel technique. NiCl$_2$·6H$_2$O (2.1 mmol) and anhydrous FeCl$_3$ (0.35 mmol) were first dissolved in ethanol (2 mL) in a vial. A solution of deionized water (DI) (0.18 mL) in ethanol (2 mL) was prepared in a separate vial. All solutions mentioned above were cooled in an ice bath for 2 h to prevent uncontrolled hydrolysis and consideration, which may lead to the formation of precipitate rather than gel formation. The Ni and Fe precursors were then mixed with an ethanol-water mixture to form a clear solution. Propylene oxide (≈ 1 mL) was then slowly added to form a gel. Finally, the prepared NiFe wet-gel was aged for 24 h to promote network formation and immersed in acetone for 5 days before the gel was vacuum dried.

I.3. Characterization. The morphologies of the catalysts were characterized by SEM (Hitachi S-4800) imaging, and energy-dispersive X-ray spectroscopy mapping operated at 1.5 kV was used to characterize the surfaces of all samples. TEM images and corresponding elemental mapping analysis were conducted using a JEM-

2100F. The electronic structure measurements were carried out using XPS (ESCALAB 250Xi). To determine the best Ni/Fe ratio in the NiFe-Boride system, we first dissolved 50 mg of the catalyst into 5 ml aqua regia through microwave digestion. Then, we took out 1 ml of sample and diluted it to 10 mL to test ICP-OES (5110).

In-situ XAS was carried out in the same condition as electrocatalytic characterization case using a modified single cell with an opening sealed by Kapton tape. The XAS signal was collected by Vortex detector in 9BM beamline of Advanced Photon Source (APS) in Argonne National Laboratory. X-ray absorption near-edge spectra (XANES) of Ni and Fe K-edge were collected by silicon drift detector at ambient air in 9BM beamline of Advanced Photon Source (APS) located in the Argonne National Laboratory.

In-situ SRXRD measurements on NiFe-Boride in a typical three-electrode setup as the same condition in electrochemical characterization case were conducted at beamline 01C2 at National Synchrotron Radiation Research Center using a specially designed acrylic container with a 1 mL of gap, sealed by Kepton tape. 16 keV of the incident X-ray (λ = 0.7749 Å) was allowed to perpendicularly transmit through the sample and electrolyte, so that the signal of synchrotron X-ray diffraction of transmission mode would be collected in a large Debye-Scherrer camera and processed using the GSAS-II software 45 to obtain plots of intensity versus 2θ.

I.4. Catalysts loaded on the electrodes. To load the catalyst on the Ni foam (thickness: 1.6 mm, Sigma), 20 mg of catalyst was dispersed in a mixture consisting of 2 mL water and 2 mL ethanol, followed by the addition of 100 µL Nafion solution. The suspension was sonicated for 30 min to prepare a homogeneous ink. Ni foam with a fixed area of 0.5×0.5 cm^2 coated with water-resistant silicone glue was drop-casted with 20 µL of the catalyst ink. Ag/AgCl (with saturated KCl as the filling solution) and platinum foil were used as the reference and counter electrodes, respectively.

I.5. Electrochemical characterization. Electrochemical measurements were performed using a three-electrode system connected to an electrochemical workstation (Autolab PGSTAT302N), equipped with built-in EIS analyzer. The working electrode was Ni foam (thickness: 1.6 mm, Sigma), which was prepared by dispersing 20 mg of catalyst in a mixture containing 1 mL water and 1 mL ethanol, followed by the addition of 100 µL Nafion solution. The suspension was sonicated for 30 min to prepare a homogeneous ink. Cyclic voltammetry (CV) measurements at 50 mV/s were performed prior to recording LSV at 1 mV/s for each sample. EIS measurements were conducted in a static solution at 1.45 V (vs. RHE). The amplitude of the sinusoidal wave was 10 mV, and the frequency scan range was between 100 kHz and 0.01 Hz. All experiments were performed at ambient temperature (23 ± 2 °C), and electrode potential was converted to the RHE scale using Eq. (5)

$$E(vs.RHE) = E(vs.Ag/AgCl) + E_{Ag/AgCl}(vs.NHE) + 0.059 \times pH \quad (5)$$

MEA test. The MEA cell is a complete CO electrolyser (Dioxide Materials) consisted of a titanium anode flow field, 904 L Stainless Steel cathode flow field, and associated nuts, bolts and insulating kit. The geometric area of each flow field is 5 cm^2, of which 45% is the channel while the rest 55% is the land area. The catalyst electrode was attached on the cathode by a copper tape, which was protected by insulating Kapton tapes to avoid electrical contact with membranes or electrolytes. A Sustainion® AEM membrane (Fumasep) was activated in 1 M aqueous KOH solution for 24 h, washed with water prior to use. The anode consisted of NiFe-Boride supported on titanium felt was prepared by a dip-coating and thermal decomposition method. The cathode is the high surface area Cu catalyst on hydrophobic carbon paper. Aqueous 2 M KOH electrolyte was used as the anolyte and was circulated using a peristaltic pump. The flow rate of the anolyte was kept at 20 mL/min. The flow rate of the CO gas flowing into the cathodic gas chamber was kept at 80 sccm by a mass flow controller. The CORR was initiated by applying a constant current density of 200 mA/cm^2, and the current density was kept constant over the course of electrolysis.

IR correction. All the polarization curves on different supports were corrected for ohmic losses (including the wiring, substrate, catalyst, and solution resistances). The iR-corrected data were given by the following equation:

$$E_{Corrected} = E - iR \quad (6)$$

where R is the series resistance of measurement, which can be obtained from an EIS Nyquist plot as the first intercept of the main arc with the axis.

ECSA. The ECSA of each catalyst was determined by measuring the electrochemical double-layer capacitances (C_{dl}) from the scan rate CV-dependence plot. The CV cycle potential window was between 0.7 and 0.8 V vs. RHE, and the scan rates were 20, 40, 60, 80, 100, and 120 mV/s. The C_{dl} was estimated $\triangle j = \frac{1}{2}(j_{charge} - J_{off\ charge})$ at the average potential in the selected range against the scan rates. The slope of the linear fit was calculated as the C_{dl}. A specific capacitance of 40 µF/cm^2 was used here. The ECSA of the catalyst was calculated by using the following equation,

$$ECSA = \frac{C_{dl}}{40\mu F/cm^2} cm^2_{ECSA} \quad (7)$$

DFT calculations. We performed the DFT calculations using the Vienna Ab Initio Simulation Package (VASP) code[38,39]. The exchange-correlation energy was modelled using Perdew-Burke-Ernzerhof (PBE) functional[40] within the generalized gradient approximation (GGA). The projector augmented-wave (PAW) pseudo-potentials[41] were used to describe the ionic cores. The cut-off energy of 450 eV was adopted after a series of tests. A Methfessel–Paxton smearing of 0.05 eV to the orbital occupation was applied for the geometry optimization and total energy computations. In all calculations, atoms at all positions were assumed to possess Hellmann-Feynman forces lower than 0.02 eV/Å, and the electronic iteration convergence criterion was 10^{-5} eV using the normal algorithm. Pourbaix diagrams were calculated using Atomic Simulation Environment (ASE)[42] with input formation energy values from Materials project[43]. Surface models for NiB$_4$O$_7$ and FeBO$_3$ were simulated by five-layer (2×2) NiB$_4$O$_7$ (100) and FeBO$_3$ (100) supercells (Supplementary Fig. 32), accompanied with a sufficient vacuum gap of 15 Å. Structural optimizations were performed on all modified slab models. We considered 4-steps intermediates adsorption to simulate the OER process (details in

below & Supplementary Fig. 33). During adsorption calculations, the top two layers were fully relaxed, while the other layers were fixed at the tested lattice position.

The reaction energies (ΔG) were obtained by

$$\Delta G = \Delta E^{DFT} + \Delta ZPE - T\Delta S \quad (8)$$

where ΔE^{DFT} is the reaction energy calculated from DFT; ΔZPE is the zero-point energy, which was neglected here; ΔS is the change in entropy, and for gaseous molecules ΔS values are obtained from the standard database in the NIST webbook[44].

Taking the reaction (1) as an example, the reaction energy is equals to

$$\Delta G^1 = G(*OH)-G(*)-G(OH^-) \quad (9)$$

where G(*OH) is the total energy of *OH adsorption configuration; G(*) is the energy of catalyst surface; G(OH$^-$) is the energy of hydroxyl ion, to calculate this value, we assume the equilibrium

$$H_2O \leftrightarrow H^+ + OH^- \quad (10)$$

which relates the chemical potentials as

$$\mu_{H^+} + \mu_{OH^-} = \mu_{H_2O} \quad (11)$$

Then,

$$\mu_{H^+} + \mu_{e^-} + \mu_{OH^-} - \mu_{e^-} = \mu_{H_2O} \quad (12)$$

Thus,

$$\mu_{OH^-} - \mu_{e^-} = \mu_{H_2O} - (\mu_{H^+} + \mu_{e^-}) \quad (13)$$

here, $\mu_{H^+} + \mu_{e^-}$ can be calculated using computational hydrogen electrode (CHE) model developed by Nørskov and co-workers[45,46]. Then, the theoretical overpotential η for OER can be calculated by

$$\eta = \max(\Delta G^i) - 1.23 \quad (14)$$

ΔG^i stands for the reaction energy for reaction (8) – (11), $i = 1, 2, 3, 4$.

Electrochemical-step symmetry index (ESSI) and maximum energy G$_{max}$ can act as a sophisticated activity descriptors for multiple-electron processes. We calculated ESSI using the following formula,

$$ESSI = \frac{1}{n}\sum_{k=1}^{n}\left(\frac{\triangle G_k^+}{e}\right) \quad (15)$$

where $\triangle G_k^+$ means all positive values of reaction energies, while negative values are not accounted.

The G$_{max}$ is the free-energy spanning from intermediate with the smallest free energy to the intermediate with the highest energy during OER.

Data availability

The data supporting this study are available within the paper and the Supplementary Information. The source data of DFT calculations are provided in this paper. All other relevant source data are available from the corresponding authors upon reasonable request. Source data are provided with this paper.

References

1. Yu, Y., Shi, Y. & Zhang, B. Synergetic transformation of solid inorganic–organic hybrids into advanced nanomaterials for catalytic water splitting. *Acc. Chem. Res.* **51**, 1711–1721 (2018).
2. You, B. & Sun, Y. Innovative strategies for electrocatalytic water splitting. *Acc. Chem. Res.* **51**, 1571–1580 (2018).
3. Yang, M. Q., Wang, J., Wu, H. & Ho, G. W. Noble metal-free nanocatalysts with vacancies for electrochemical water splitting. *Small* **14**, e1703323 (2018).
4. Wang, Y. & Yan, D. El Hankari, S., Zou, Y. & Wang, S. Recent progress on layered double hydroxides and their derivatives for electrocatalytic water splitting. *Adv. Sci.* **5**, 1800064 (2018).
5. Li, H. et al. Earth-abundant iron diboride (FeB2) nanoparticles as highly active bifunctional electrocatalysts for overall water splitting. *Adv. Energy Mater.* **7**, 1700513 (2017).
6. Yu, F. et al. High-performance bifunctional porous non-noble metal phosphide catalyst for overall water splitting. *Nat. Commun.* **9**, 2551 (2018).
7. Panda, C. et al. From a molecular 2Fe-2Se precursor to a highly efficient Iron diselenide electrocatalyst for overall water splitting. *Angew. Chem. Int. Ed.* **56**, 10506–10510 (2017).
8. Yang, Y. et al. MoS2–Ni3S2 heteronanorods as efficient and stable bifunctional electrocatalysts for overall water splitting. *ACS Catal.* **7**, 2357–2366 (2017).
9. Shiva Kumar, S. & Himabindu, V. Hydrogen production by PEM water electrolysis – A review. *Mater. Sci. Energy Technol.* **2**, 442–454 (2019).

10. Jouny, M., Luc, W. & Jiao, F. General techno-economic analysis of CO2 electrolysis systems. *Ind. Eng. Chem. Res.* **57**, 2165–2177 (2018).
11. Bediako, D. K., Surendranath, Y. & Nocera, D. G. Mechanistic studies of the oxygen evolution reaction mediated by a nickel-borate thin film electrocatalyst. *J. Am. Chem. Soc.* **135**, 3662–3674 (2013).
12. Masa, J. et al. Amorphous cobalt boride (Co2B) as a highly efficient nonprecious catalyst for electrochemical water splitting: oxygen and hydrogen evolution. *Adv. Energy Mater.* **6**, 1502313 (2016).
13. Nsanzimana, J. M. V. et al. Ultrathin amorphous iron–nickel boride nanosheets for highly efficient electrocatalytic oxygen production. *Chem. Eur. J.* **24**, 18502–18511 (2018).
14. Su, L. et al. Borate-ion intercalated NiFe layered double hydroxide to simultaneously boost mass transport and charge transfer for catalysis of water oxidation. *J. Colloid Interface Sci.* **528**, 36–44 (2018).
15. Gupta, S., Patel, M. K., Miotello, A. & Patel, N. Metal boride-based catalysts for electrochemical water-splitting: A review. *Adv. Funct. Mater.* **30**, 1906481 (2020).
16. Mabayoje, O., Shoola, A., Wygant, B. R. & Mullins, C. B. The role of anions in metal chalcogenide oxygen evolution catalysis: electrodeposited thin films of nickel sulfide as "pre-catalysts". *ACS Energy Lett.* **1**, 195–201 (2016).
17. Nsanzimana, J. M. V. et al. Facile synthesis of amorphous ternary metal borides–reduced graphene oxide hybrid with superior oxygen evolution activity. *ACS Appl. Mater. Interfaces* **11**, 846–855 (2019).
18. Xu, X., Song, F. & Hu, X. A nickel iron diselenide-derived efficient oxygen-evolution catalyst. *Nat. Commun.* **7**, 1–7 (2016).
19. De Luna, P. et al. What would it take for renewably powered electrosynthesis to displace petrochemical processes? *Science* **364**, 6438 (2019).
20. Bajdich, M., Garcia-Mota, M., Vojvodic, A., Norskov, J. K. & Bell, A. T. Theoretical investigation of the activity of cobalt oxides for the electrochemical oxidation of water. *J. Am. Chem. Soc.* **135**, 13521–13530 (2013).
21. Dickens, C. F., Kirk, C. & Nørskov, J. K. Insights into the electrochemical oxygen evolution reaction with ab Initio calculations and microkinetic modeling: Beyond the limiting potential volcano. *J. Phys. Chem. C.* **123**, 18960–18977 (2019).
22. Rossmeisl, J., Logadottir, A. & Nørskov, J. K. Electrolysis of water on (oxidized) metal surfaces. *Chem. Phys.* **319**, 178–184 (2005).
23. Koper, M. T. Analysis of electrocatalytic reaction schemes: distinction between rate-determining and potential-determining steps. *J. Solid State Electrochem* **17**, 339–344 (2013).
24. Romain, S., Bozoglian, F., Sala, X. & Llobet, A. Oxygen– oxygen bond formation by the Ru-Hbpp water oxidation catalyst occurs solely via an intramolecular reaction pathway. *J. Am. Chem. Soc.* **131**, 2768–2769 (2009).
25. Govindarajan, N., García-Lastra, J. M., Meijer, E. J. & Calle-Vallejo, F. Does the breaking of adsorption-energy scaling relations guarantee enhanced electrocatalysis? *Curr. Opin. Electrochem* **8**, 110–117 (2018).
26. Exner, K. S. A universal descriptor for the screening of electrode materials for multiple-electron processes: beyond the thermodynamic overpotential. *ACS Catal.* **10**, 12607–12617 (2020).
27. Exner, K. S. Why approximating electrocatalytic activity by a single free-energy change is insufficient. *Electrochim. Acta* **375**, 137975 (2021).
28. Masa, J. et al. Ultrathin high surface area nickel boride (NixB) nanosheets as highly efficient electrocatalyst for oxygen evolution. *Adv. Energy Mater.* **7**, 1700381 (2017).
29. Görlin, M. et al. Oxygen evolution reaction dynamics, faradaic charge efficiency, and the active metal redox states of Ni–Fe oxide water splitting electrocatalysts. *J. Am. Chem. Soc.* **138**, 5603–5614 (2016).
30. Wang, H. Y. et al. Ni3+-inducedformation of active NiOOH on the spinel Ni–Co oxide surface for efficient oxygen evolution reaction. *Adv. Energy Mater.* **5**, 1500091 (2015).
31. Hung, S.-F. et al. In situ spatially coherent identification of phosphide-based catalysts: crystallographic latching for highly efficient overall water electrolysis. *ACS Energy Lett.* **4**, 2813–2820 (2019).
32. Weng, B. et al. A layered Na1−xNiyFe1−yO2 double oxide oxygen evolution reaction electrocatalyst for highly efficient water-splitting. *Energy Environ. Sci.* **10**, 121–128 (2017).
33. Hong, W., Sun, S., Kong, Y., Hu, Y. & Chen, G. NixFe1−xB nanoparticle self-modified nanosheets as efficient bifunctional electrocatalysts for water splitting: experiments and theories. *J. Mater. Chem. A* **8**, 7360–7367 (2020).
34. Wang, X. et al. Self-constructed multiple plasmonic hotspots on an individual fractal to amplify broadband hot electron generation. *ACS Nano* **15**, 10553–10564 (2021).
35. Marshall, A. T. & Vaisson-Béthune, L. Avoid the quasi-equilibrium assumption when evaluating the electrocatalytic oxygen evolution reaction mechanism by Tafel slope analysis. *Electrochem. Commun.* **61**, 23–26 (2015).
36. Sun, S. et al. Switch of the rate-determining step of water oxidation by spin-selected electron transfer in spinel oxides. *Chem. Mater.* **31**, 8106–8111 (2019).
37. Li, H. et al. Amorphous nickel-cobalt complexes hybridized with 1T-phase molybdenum disulfide via hydrazine-induced phase transformation for water splitting. *Nat. Commun.* **8**, 15377 (2017).
38. Kresse, G. & Hafner, J. Ab initio molecular dynamics for liquid metals. *Phys. Rev. B* **47**, 558 (1993).
39. Kresse, G. & Furthmüller, J. Efficient iterative schemes for ab initio total-energy calculations using a plane-wave basis set. *Phys. Rev. B* **54**, 11169 (1996).
40. Perdew, J. P., Burke, K. & Ernzerhof, M. Generalized gradient approximation made simple. *Phys. Rev. Lett.* **77**, 3865 (1996).
41. Payne, M. C., Teter, M. P., Allan, D. C., Arias, T. & Joannopoulos, A. J. Iterative minimization techniques for ab initio total-energy calculations: molecular dynamics and conjugate gradients. *Rev. Mod. Phys.* **64**, 1045 (1992).
42. Larsen, A. H. et al. The atomic simulation environment-a Python library for working with atoms. *J. Phys.: Condens. Matter* **29**, 273002 (2017).
43. Jain, A., Castelli, I. E., Hautier, G., Bailey, D. H. & Jacobsen, K. W. Performance of genetic algorithms in search for water splitting perovskites. *J. Mater. Sci.* **48**, 6519–6534 (2013).
44. Chase, M. W. NIST-JANAF thermochemical tables for oxygen fluorides. *J. Phys. Chem. Ref. Data.* **25**, 551–603 (1996).
45. Rossmeisl, J., Qu, Z.-W., Zhu, H., Kroes, G.-J. & Nørskov, J. K. Electrolysis of water on oxide surfaces. *J. Electroanal. Chem.* **607**, 83–89 (2007).
46. Nørskov, J. K. et al. Origin of the overpotential for oxygen reduction at a fuel-cell cathode. *J. Phys. Chem. B* **108**, 17886–17892 (2004).
47. Cai, W. et al. Amorphous versus crystalline in water oxidation catalysis: A case study of NiFe alloy. *Nano Lett.* **20**, 4278–4285 (2020).
48. Zou, Y. et al. 3D hierarchical heterostructure assembled by NiFe LDH/(NiFe)Sx on biomass-derived hollow carbon microtubes as bifunctional electrocatalysts for overall water splitting. *Electrochim. Acta* **348**, 136339 (2020).
49. Chen, G. et al. An amorphous nickel-iron-based electrocatalyst with unusual local structures for ultrafast oxygen evolution reaction. *Adv. Mater.* **31**, 1900883 (2019).
50. Zhou, Y. et al. Exceptional performance of hierarchical Ni-Fe (hydr)oxide@NiCu electrocatalysts for water splitting. *Adv. Mater.* **31**, 1806769 (2019).
51. Teng, X. et al. Self-Growing NiFe-Based hybrid nanosheet arrays on Ni nanowires for overall water aplitting. *ACS Appl. Energy Mater.* **2**, 5465–5471 (2019).
52. Qiu, Z., Tai, C.-W., Niklasson, G. A. & Edvinsson, T. Direct observation of active catalyst surface phases and the effect of dynamic self-optimization in NiFe-layered double hydroxides for alkaline water splitting. *Energy Environ. Sci.* **12**, 572–581 (2019).
53. Zhang, P. et al. Dendritic core-shell nickel-iron-copper metal/metal oxide electrode for efficient electrocatalytic water oxidation. *Nat. Commun.* **9**, 1–10 (2018). 381.
54. Zhang, J. et al. Single-atom Au/NiFe layered double hydroxide electrocatalyst: probing the origin of activity for oxygen evolution reaction. *J. Am. Chem. Soc.* **140**, 3876–3879 (2018).
55. Dong, C., Kou, T., Gao, H., Peng, Z. & Zhang, Z. Eutectic-Derived mesoporous Ni-Fe-O nanowire network catalyzing oxygen evolution and overall water splitting. *Adv. Energy Mater.* **8**, 1701347 (2018).
56. Zhang, H. et al. Bifunctional heterostructure assembly of NiFe LDH nanosheets on NiCoP nanowires for highly efficient and stable overall water splitting. *Adv. Funct. Mater.* **28**, 1706847 (2018).
57. Cai, Z. et al. Introducing Fe(2+) into Nickel-Iron layered double hydroxide: local structure modulated water oxidation activity. *Angew. Chem.* **57**, 9392–9396 (2018).
58. He, T. et al. Synthesis of amorphous boride nanosheets by the chemical reduction of Prussian blue analogs for efficient water electrolysis. *J. Mater. Chem. A* **6**, 23289–23294 (2018).

Author contributions

H.Y.L. and E.H.S. supervised the project. N.W. conceived the idea and carried out the experiments. N.W., H.Y.L., and E.H.S. wrote the paper. A.X. P.O., and Z.W. carried out

Competing interests

The authors declare no competing interests.

Additional information

Supplementary information The online version contains supplementary material available at https://doi.org/10.1038/s41467-021-26307-7.

Correspondence and requests for materials should be addressed to Yongchang Liu, Edward H. Sargent or Hongyan Liang.

Peer review information *Nature Communications* thanks Abdoulaye Djire, Kai Exner, Justus Masa, and the other, anonymous, reviewers for their contributions to the peer review of this work.

Reprints and permission information is available at http://www.nature.com/reprints

Publisher's note Springer Nature remains neutral with regard to jurisdictional claims in published maps and institutional affiliations.